Electronic excitations in $5d^4 \, J = 0 \, Os^{4+}$ halides studied by resonant inelastic x-ray scattering and optical spectroscopy

P. Warzanowski [1], M. Magnaterra [1], P. Stein [1], G. Schlicht [1], Q. Faure [2,3], Ch. J. Sahle [2], T. Lorenz [1], P. Becker [4], L. Bohatý,[4] M. Moretti Sala [5], G. Monaco [6], P. H. M. van Loosdrecht [1], and M. Grüninger [1]

[1]*Institute of Physics II, University of Cologne, 50937 Cologne, Germany*
[2]*ESRF, The European Synchrotron, 71 Avenue des Martyrs, CS40220, 38043 Grenoble Cedex 9, France*
[3]*Laboratoire Léon Brillouin, CEA, Centre National de la Recherche Scientifique, Université Paris-Saclay,*
CEA-Saclay, 91191 Gif-sur-Yvette, France
[4]*Sect. Crystallography, Institute of Geology and Mineralogy, University of Cologne, 50674 Cologne, Germany*
[5]*Dipartimento di Fisica, Politecnico di Milano, I-20133 Milano, Italy*
[6]*Dipartimento di Fisica e Astronomia "Galileo Galilei," Università di Padova, I-35121 Padova, Italy*

We demonstrate that the cubic antifluorite-type halides K_2OsCl_6, K_2OsBr_6, and Rb_2OsBr_6 are excellent realizations of nonmagnetic $J = 0$ compounds. The magnetic susceptibility shows the corresponding Van Vleck type of behavior and no sign of defects. We investigate the electronic excitations with two complementary techniques, resonant inelastic x-ray scattering and optical spectroscopy. This powerful combination allows us to thoroughly study, e.g., on-site intra-t_{2g} excitations and t_{2g}-to-e_g excitations as well as intersite excitations across the Mott gap and an exciton below the gap. In this way, we determine the electronic parameters with high accuracy, altogether yielding a comprehensive picture. In K_2OsCl_6, we find the spin-orbit coupling constant $\zeta = 0.34$ eV, Hund's coupling $J_H = 0.43$ eV, the onset of excitations across the Mott gap at $\Delta = 2.2$ eV, the cubic crystal-field splitting $10Dq = 3.3$ eV, and the charge-transfer energy $\Delta_{CT} = 4.6$ eV. With $J_H/\zeta = 1.3$, K_2OsCl_6 is in the intermediate-coupling regime. In a t_{2g}-only Kanamori picture, the above values correspond to $\zeta^{eff} = 0.41$ eV and $J_H^{eff} = 0.28$ eV, which is very close to results reported for related $5d^4$ iridates. In the tetragonal phase at 5 K, the noncubic crystal field causes a peak splitting of the $J = 1$ state as small as 4 meV. Compared to K_2OsCl_6, the bromides K_2OsBr_6 and Rb_2OsBr_6 show about 12–14% smaller values of $10Dq$ and Δ_{CT}, while the spin-orbit entangled intra-t_{2g} excitations below 2 eV and hence ζ and J_H are reduced by less than 4%. Furthermore, the Mott gap in K_2OsBr_6 is reduced to about 1.8 eV.

I. INTRODUCTION

The family of $5d$ transition-metal compounds features Mott-insulating quantum materials in which strong spin-orbit coupling plays the central role [1–5]. Prominent examples are t_{2g}^5 iridates with spin-orbit entangled $J = 1/2$ moments [6–8]. Compounds with edge-sharing IrO_6 octahedra have been predicted to show bond-directional Kitaev-type exchange couplings [9]. This has raised hopes to realize the Kitaev model on tricoordinated lattices, where strong exchange frustration yields an intriguing quantum spin liquid [10–12]. Experimentally, the dominant bond-directional character of exchange interactions has been demonstrated for honeycomb Na_2IrO_3 [13,14]. Remarkably, Kitaev exchange has been found to have a very different effect for $J = 1/2$ moments on an fcc lattice with corner-sharing IrO_6 octahedra as realized in the double perovskite Ba_2CeIrO_6. There, antiferromagnetic Kitaev coupling counteracts the geometric frustration of isotropic Heisenberg exchange [15]. For face-sharing IrO_6 octahedra as in the Ir_2O_9 dimer compounds $Ba_3MIr_2O_9$, spin-orbit coupling competes with strong intradimer hopping that yields quasimolecular orbitals. Still, resonant inelastic x-ray scattering (RIXS) studies for $M = Ce^{4+}$ and In^{3+} established the spin-orbit entangled $J_{dim} = 0$ and $3/2$

character of the respective quasimolecular magnetic moments [16,17].

For a t_{2g}^4 configuration in cubic symmetry, dominant spin-orbit coupling ζ is expected to yield a nonmagnetic $J = 0$ ground state. However, strong exchange interactions give rise to a dispersion of magnetic excited states, and if the dispersion is large enough, these may condense and drive magnetism of excitonic Van Vleck type that is also called singlet magnetism [18–22]. In this scenario, a magnetic amplitude mode equivalent to a Higgs mode is expected, which has been proposed for antiferromagnetic Ca_2RuO_4 [18,23]. In this layered $4d^4$ compound, one has to consider the tetragonal crystal-field splitting Δ_{CF} [21,24–33] and that spin-orbit coupling is smaller than in $5d$ materials such that the physics is governed by the ratio $\Delta_{CF}/\zeta > 2$ [32,33]. For dominant noncubic Δ_{CF}, d^4 compounds turn into spin $S = 1$ magnets. Considering (nearly) cubic symmetry, the local intra-t_{2g} excitations from the $J = 0$ state have been studied by RIXS in $4d^4$ K_2RuCl_6 [34] and in the $5d^4$ Ir^{5+} double perovskites A_2BIrO_6 ($A =$ Ba, Sr; $B =$ Y, Gd, Lu, Sc) [35–39]. Among these, Sr_2YIrO_6 and Ba_2YIrO_6 were reported to host magnetic order [40,41] which has been attributed to the presence of $5d^5$ Ir^{4+} and $5d^3$ Ir^{6+} defects [42]. Pyrochlore $Yb_2Os_2O_7$ with $5d^4$ Os^{4+} ions exhibits a

trigonal distortion and a defect-induced magnetic response
[43]. For K_2RuCl_6, the possible role of vibronic effects has
been discussed [44].

Here, we employ RIXS at the Os L_3 edge and optical
spectroscopy to study stoichiometric single crystals of the
$5d^4$ halides K_2OsCl_6 and A_2OsBr_6 with $A =$ K and Rb. In
the magnetic susceptibility, we do not find any indication of
magnetic defects. Our results establish these materials as a ref-
erence for $J = 0$ systems in the intermediate regime between
LS coupling for $J_H/\zeta \to \infty$ and jj coupling for $J_H/\zeta \to 0$.
We show that $J_H/\zeta = 1.3$ is equivalent to $J_H^{\mathrm{eff}}/\zeta^{\mathrm{eff}} = 0.8$ in
the Kanamori scheme [45], which considers only t_{2g} orbitals.
Our result for $J_H^{\mathrm{eff}}/\zeta^{\mathrm{eff}}$ is in excellent agreement with the
values reported for $5d^4$ iridates [35–38]. The antifluorite-
type Os compounds combine several properties which are
advantageous for a precise determination of the electronic
parameters. At room temperature, they show cubic symmetry
[46–48], and for the purpose of studying the local electronic
excitations the compounds may be viewed as being composed
of undistorted, well-separated OsX_6 octahedra with, to first
approximation, negligible interactions between them. This
yields well-defined, narrow RIXS peaks even at high energy
such as the charge-transfer excitations at 4.6, 5.7, and 8.0 eV
in K_2OsCl_6, allowing for a straightforward determination of
the charge-transfer energy Δ_{CT}.

For the study of orbital and electronic excitations in Mott
insulators, RIXS and optical spectroscopy are complemen-
tary techniques. In the case of inversion symmetry, RIXS at
the transition-metal L edge is in particular sensitive to lo-
cal, parity-conserving excitations between d orbitals [32,34–
37,43,49]. In contrast, optical spectroscopy is most sensitive
to electric dipole active absorption features such as inter-site
excitations across the Mott gap or excitons [33,50,51], while
local excitations between d orbitals mainly contribute in a
phonon-assisted process, i.e., they become electric dipole ac-
tive by the simultaneous excitation of a symmetry-breaking
phonon [52–55]. Interesting examples studied by both tech-
niques are, e.g., the $3d^2$ vanadates $R\mathrm{VO}_3$ [51,55,56] or the ex-
citations from $J = 1/2$ to $3/2$ in the $4d^5$ Kitaev material $\alpha -$
RuCl_3 [57–59]. In the infrared data, weak phonon-assisted
absorption features can only be detected in the transparent
range with excitation energies smaller than the Mott gap.
In comparison, RIXS offers the possibility to observe the
corresponding orbital excitations also for larger excitation
energies but with limited energy resolution. At the Os L_3
edge with an incident energy $E_{\mathrm{in}} = 10.870$ keV, we achieve a
resolution $\delta E = 63$ meV, i.e., $\delta E/E_{\mathrm{in}} \approx 6 \times 10^{-6}$. In contrast,
the Fourier spectrometer employed for infrared measurements
offers a resolution better than 0.1 meV. Accordingly, it is more
difficult to determine the electronic parameters by using only
one of the two techniques, as discussed, e.g., for RIXS on
$\mathrm{Yb}_2\mathrm{Os}_2\mathrm{O}_7$ [43] or infrared spectroscopy on K_2OsCl_6 [60]. For
K_2OsCl_6, we will show below that the combination of the two
techniques resolves all ambiguities.

II. SINGLE-CRYSTAL GROWTH AND CRYSTAL STRUCTURE

Single crystals of K_2OsCl_6 and of the bromides A_2OsBr_6
with $A =$ K and Rb were grown starting from commercially
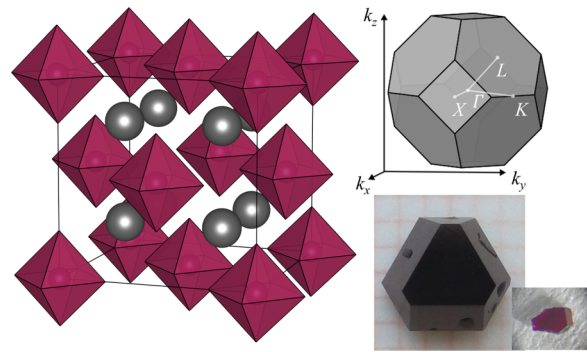
FIG. 1. Left: Face-centered cubic crystal structure of A_2OsX_6 at
300 K. The OsX_6 octahedra ($X =$ Cl, Br) are plotted in red and
the A^+ ions ($A =$ K, Rb) are shown in gray. Top right: Sketch of
the first Brillouin zone of the fcc lattice with the high-symmetry
points Γ, X, K, and L. Lower right: Photos of a K_2OsBr_6 crys-
tal and of the thin, transparent sample of K_2OsCl_6 that has been
studied in infrared transmittance. The size of the latter amounts to
$\approx 0.5\,\mathrm{mm} \times 0.3\,\mathrm{mm} \times 0.12\,\mathrm{mm}$.

available dihydrogen hexahalogenoosmate (IV) $\mathrm{H}_2\mathrm{OsCl}_6$, re-
spectively $\mathrm{H}_2\mathrm{OsBr}_6$, and the respective halide KCl or ABr.
The educts were dissolved in a stoichiometric ratio in diluted
hydrochloric (respectively hydrobromic) acid. For the potas-
sium compounds, single crystals of several millimeters size
were achieved by slow, controlled evaporation of the solvent
at 293 K during a typical growth period of one to two weeks.
For the Rb compound, crystals were of submillimeter size due
to the low solubility. Examples of K_2OsBr_6 and K_2OsCl_6 are
shown in Fig. 1.

At room temperature, these K_2PtCl_6-type compounds show
a cubic crystal structure with space group $Fm\bar{3}m$ [46–48]
(see Fig. 1). The Os^{4+} ions are located on an fcc lattice. The
stoichiometry of all three compounds has been verified on
small crystals by x-ray diffraction in the cubic phase [61].
At 45 K, K_2OsCl_6 exhibits a phase transition to a tetragonal
phase [47]. For K_2OsBr_6, the structural transition at 220 K
to a phase with tetragonal symmetry is followed by a phase
transition to a monoclinic phase at 200 K [48].

III. MAGNETIC SUSCEPTIBILITY

The magnetic susceptibility χ of K_2OsCl_6 and K_2OsBr_6 is
plotted in Fig. 2. We observe a temperature-independent sus-
ceptibility without any indication of a Curie-Weiss contribu-
tion of defects. The constant value $\chi = 7.5 \times 10^{-4}$ emu/mol
can be attributed to a dominant Van Vleck term and a
small diamagnetic contribution of the closed shells of K^+,
Os^{4+}, Cl^-, and Br^-, $\chi = \chi_{\mathrm{VV}} + \chi_{\mathrm{dia}}$. Via tabulated values
[62], we estimate $\chi_{\mathrm{dia}}^{\mathrm{Cl}} = -2.1 \times 10^{-4}$ emu/mol and $\chi_{\mathrm{dia}}^{\mathrm{Br}} =
-2.7 \times 10^{-4}$ emu/mol. This yields experimental values of
the Van Vleck contribution of $\chi_{\mathrm{VV}}^{\mathrm{Cl}} = 9.6 \times 10^{-4}$ emu/mol
and $\chi_{\mathrm{VV}}^{\mathrm{Br}} = 10.2 \times 10^{-4}$ emu/mol.

Our spectroscopic data establish a $J = 0$ ground state
of the $5d^4$ configuration of Os^{4+} (see Sec. V), in agree-
ment with predictions of density functional theory [63]. The
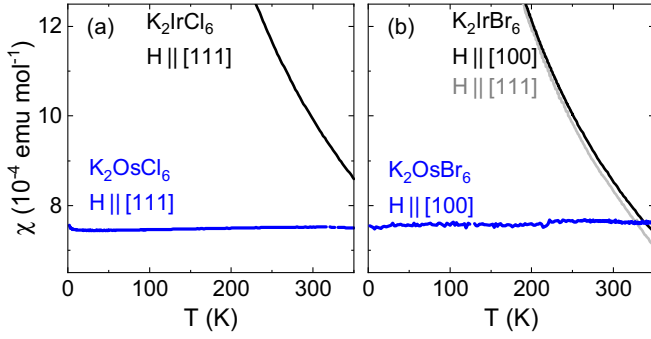
FIG. 2. Magnetic susceptibility χ of K_2OsCl_6 and K_2OsBr_6. Both compounds show dominant temperature-independent Van Vleck paramagnetism. For comparison, we show χ of the $J = 1/2$ iridium sister compounds with a sizable Curie-Weiss contribution.

corresponding Van Vleck susceptibility is given by

$$\chi_{VV} = \frac{N}{V} 2\mu_B^2 \sum_n \frac{|\langle n|L_z + gS_z|0\rangle|^2}{E_n - E_0}, \qquad (1)$$

where $|0\rangle$ and $|n\rangle$ denote the ground state and excited states, respectively, $E_n - E_0$ is the respective energy difference, S_z and L_z refer to the z components of spin and orbital angular momentum, μ_B is the Bohr magneton, and N/V denotes the density of Os ions. In the most simple picture, one can consider only the matrix elements from the $J = 0$ ground state to the lowest excited state, the $J = 1$ triplet, assuming that all other excitation energies are infinite. Only the matrix element to the $J_z = 0$ state of the triplet is finite. Using an $|M_S, M_L\rangle$ basis [18], the relevant states are $|0\rangle = (|1, -1\rangle - |0, 0\rangle + |-1, 1\rangle)/\sqrt{3}$ and $|1\rangle = (|1, -1\rangle - |-1, 1\rangle)/\sqrt{2}$. With $\mathbf{M} = 2\mathbf{S} - \mathbf{L}$ [18] for the t_{2g} states with $L_{eff} = -1$, the corresponding matrix element equals $|\langle 1|L_z - 2S_z|0\rangle|^2 = 6$. With an excitation energy of 0.35 eV (see below), this yields $\chi_{VV}^{J=1} = 11 \times 10^{-4}$ emu/mol. As a more sophisticated alternative, we calculate the matrix elements via QUANTY [64,65], using the electronic parameters that result from our thorough analysis of the spectroscopic data discussed below. For the 209 possible excited states of a $5d^4$ configuration, we find that only two states contribute significantly. About 90% arise from the $J = 1$ state at about 0.35 eV, while 10% stem from a state with one electron in the e_g orbitals at about 3.5 eV. The two matrix elements are similar, hence the contribution of the second term is suppressed by about a factor 10 due to the higher excitation energy. We find $\chi_{VV,mod}^{Cl} = 8.8 \times 10^{-4}$ emu/mol and $\chi_{VV,mod}^{Br} = 8.6 \times 10^{-4}$ emu/mol, in reasonable agreement with the experimental result.

IV. SPECTROSCOPIC MEASUREMENTS

All RIXS experiments were performed at beamline ID20 of the European Synchrotron Radiation Facility. Incident photons from three consecutive U26 undulators were monochromatized by a Si(111) high-heat-load monochromator and either a successive Si(664) backscattering-channel-cut or a Si(311) channel-cut postmonochromator at 10.870 keV with a final bandwidth of 18 meV or 0.29 eV, respectively. The monochromatic x-ray beam was focused by a mirror system

in Kirkpatrick-Baez geometry to 8×50 μm^2 (V × H) at the sample position. Incident π polarization in the horizontal scattering plane was used. We specify the transferred momentum **q** in reciprocal lattice units. First, we studied the resonance behavior of K_2OsCl_6 at the Os L_3 edge by measuring low-energy-resolution RIXS spectra with the incident energy in the range from 10.866 to 10.880 keV. Then, the incident energy was tuned to 10.870 keV to maximize the intra-t_{2g} excitations. RIXS spectra were measured using the 2 m analyzer/detector arm of the spectrometer. The Si(6,6,4) reflection of a diced Si(5,5,3) analyzer crystal was utilized in conjunction with a pixelated area detector [66–68]. The overall energy resolution of the setup was 63 meV for the high-energy-resolution spectra and 0.29 eV for the low-energy-resolution spectra, respectively, as estimated by the full width at half maximum of quasielastic scattering from a piece of adhesive tape. To determine the energy-loss scale of the spectrometer, we first define its origin at the center of mass of the rocking curve of a diced Si(664) analyzer crystal using quasielastic scattering from a piece of adhesive tape. Then, the increment of the scale is determined mainly by the analyzer Bragg angle and detector position. The combination of RIXS and optics allows us to examine the accuracy of this approach up to high energies. Comparing the excitation energy of a RIXS peak with the corresponding feature in the optical data at 2117 meV (see below), we find that the two values agree within about 1%. This excellent result is in line with a previous study of the precision of the RIXS energy scale for energies up to 150 meV [69]. For a consistent analysis, we have anchored the RIXS energy-loss scale using the optical value of 2117 meV. The RIXS measurements were performed using a dynamic helium gas flow cryostat as described elsewhere [70]. RIXS data were collected at 20 and 300 K on a (111) surface, with (001) and (110) lying in the horizontal scattering plane. All RIXS spectra are corrected for energy-dependent self-absorption [71].

In the complex optical conductivity $\sigma(\omega) = \sigma_1(\omega) + i\sigma_2(\omega)$, we address very weak absorption features as well as strong ones. This requires two different approaches [50,72,73]. For the strong absorption bands above the Mott gap, we performed ellipsometry measurements on a shiny (111) surface of a K_2OsCl_6 crystal at 300 K in the range from 1 to 6 eV using a Woollam VASE ellipsometer. The ellipsometric data of a cubic single crystal directly yield $\sigma(\omega)$ [74]. In the transparent range below the gap, the transmittance $T(\omega)$ is the appropriate tool, and we obtain complex $\sigma(\omega)$ via determining the complex index of refraction $n(\omega) + i\kappa(\omega)$ with $\kappa \ll n$ and $\sigma_1 \propto n\kappa$ [75]. In particular, $T(\omega)$ depends exponentially on $\kappa(\omega)$, offering high sensitivity. The real part $n(\omega)$ is dominated by contributions from strong absorption bands at higher energy while the weak absorption features leave only very small signatures in $n(\omega)$. For our purpose, $n(\omega)$ can reasonably be approximated as a constant that we derive from the period of the Fabry-Pérot interference fringes in $T(\omega)$ which arise from multiple reflections within the sample. We measured $T(\omega)$ from 0.1 to 2.5 eV at several temperatures in the range from 5 to 300 K using a Bruker IFS 66/v Fourier-transform spectrometer equipped with a continuous-flow ^{4}He cryostat. We employed thin plane-parallel samples with a cubic (111) surface. The sample of K_2OsCl_6 was lapped to
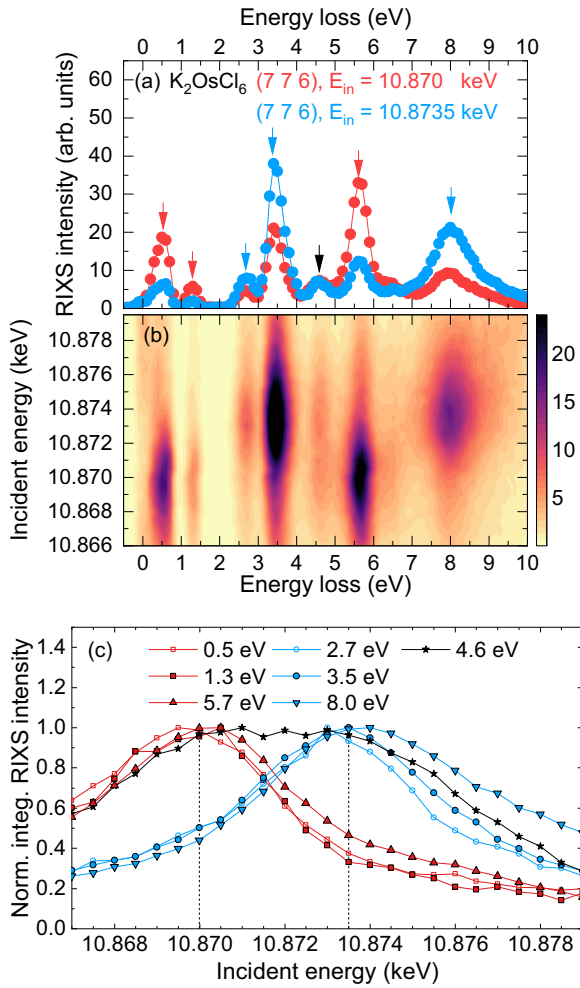
FIG. 3. Resonance behavior of K_2OsCl_6 at $T = 20$ K. (a) Low-resolution RIXS spectra for incident energy $E_{in} = 10.870$ keV and 10.8735 keV, i.e., at t_{2g} and e_g resonance, respectively. Arrows indicate peak energies and their color symbolizes the resonance behavior. (b) Low-resolution resonance map of the RIXS intensity based on RIXS spectra measured with different E_{in} for $\mathbf{q} = (7\ 7\ 6)$. (c) Normalized integrated intensity of the RIXS peaks as a function of E_{in}. The integration interval is chosen to be ± 0.4 eV around the peak energy. With the exception of the 4.6 eV peak, all peaks show either t_{2g} or e_g resonance.

a suitable thickness and polished with CeO_2 in propanol, while the sample of K_2OsBr_6 was measured as grown. The sample thickness amounts to $d = 120(5)$ μm for K_2OsCl_6 and $d = 170(7)$ μm for K_2OsBr_6.

V. RESULTS ON K_2OsCl_6

A. Resonance behavior

To study the resonance behavior and to maximize the RIXS intensity, we collected low-resolution RIXS spectra of K_2OsCl_6 for different incident energies at $T = 20$ K for a transferred momentum $\mathbf{q} = (7\ 7\ 6)$ [see Fig. 3(b)]. With the energy loss being independent of E_{in} for all of the observed RIXS peaks, we find the two distinct resonance energies $E_{in} = 10.870$ keV and 10.8735 keV, as shown in Fig. 3(c). These can

be attributed to t_{2g} resonance and e_g resonance, i.e., resonance enhancement of the initial x-ray absorption part of the RIXS process in which a $2p$ core electron is promoted to either a t_{2g} or an e_g orbital, respectively. The difference of the two resonance energies gives a first estimate of the cubic crystal-field splitting $10Dq \approx 3.5$ eV. This agrees with the strong RIXS peak at about 3.5 eV energy loss that exhibits e_g resonance behavior and corresponds to an excitation from a t_{2g} orbital to an e_g orbital. Cuts of the resonance map at the two resonance energies are shown in Fig. 3(a).

B. Character of RIXS features

Based on the resonance behavior, we distinguish three different kinds of excitations: intra-t_{2g} excitations, crystal-field excitations to e_g orbitals, and charge-transfer excitations. At low energy loss, up to about 2 eV, all RIXS features exhibit t_{2g} resonance and can be attributed to intra-t_{2g} excitations. Their excitation energies mainly reflect spin-orbit coupling ζ and Hund's coupling J_H. These intra-t_{2g} excitations will be addressed below by high-resolution RIXS measurements and optical transmission measurements. At higher energy loss, the RIXS peaks in the range from 2.7 to 4.6 eV are resonantly enhanced for $E_{in} = 10.8375$ keV and correspond to crystal-field excitations to e_g orbitals, $|t_{2g}^4\rangle \rightarrow |t_{2g}^3 e_g^1\rangle$. We will show below that the lowest e_g excitation at 2.7 eV can be identified with the high-spin $S = 2$ multiplet with ^5E symmetry. The energy of this high-spin state is reduced by Hund's coupling J_H, and the ^5E multiplet becomes the d^4 ground state if J_H dominates over the cubic crystal-field splitting $10Dq$.

At still higher energy loss, we observe charge-transfer excitations, $|5d_{Os}^4 3p_{Cl}^6\rangle \rightarrow |5d_{Os}^5 3p_{Cl}^5\rangle$. The peaks at 4.6 and 5.7 eV both show t_{2g} resonance and hence can be attributed to $|t_{2g}^5 3p_{Cl}^5\rangle$ final states. Roughly, these two excited states with t_{2g}^5 configuration can be identified with $J = 1/2$ and $3/2$ on the Os site. The peak at 8.0 eV energy loss shows e_g resonance and corresponds to excitations from Cl $3p$ to Os $5d$ e_g orbitals. The RIXS peak at 4.6 eV is the only one that resonates at both 10.870 and 10.8735 keV (see lower panel of Fig. 3). This suggests an overlap between an on-site crystal-field excitation to e_g orbitals and the lowest charge-transfer excitation to t_{2g} orbitals. Note that the energy difference of about 3.4 eV between the peaks at 8.0 and 4.6 eV confirms our first rough estimate of $10Dq \approx 3.5$ eV. Accordingly, we identify the peak energy of the lowest charge-transfer excitation with the charge-transfer energy, $\Delta_{CT} = 4.6$ eV.

The occurrence of both t_{2g} resonance and e_g resonance behavior of charge-transfer excitations has previously been observed in, e.g., $5d^5$ K_2IrBr_6 [76], $5d^4$ $Yb_2Os_2O_7$ [43], and $5d^2$ Ba_2YReO_6 [35]. In the present case of K_2OsCl_6, the charge-transfer excitations are particularly well defined and yield comparably narrow RIXS peaks. For instance the 5.7 eV peak shows a full width at half maximum of 0.6 eV. This suggests that the charge-transfer excitations to t_{2g} orbitals are well localized in nonmagnetic K_2OsCl_6, in agreement with the notion that interactions between the well-separated $OsCl_6$ octahedra are very small, at least for t_{2g} orbitals.
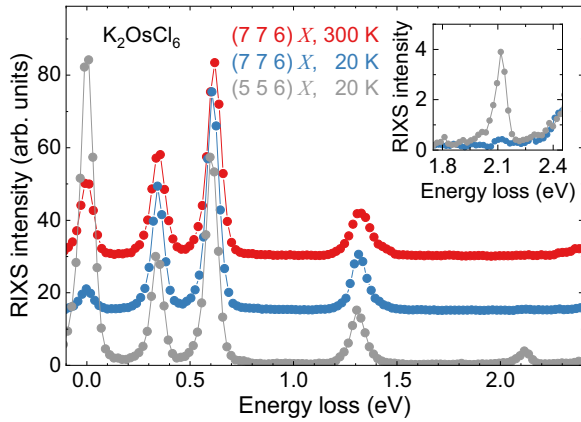
FIG. 4. Intra-t_{2g} excitations of K_2OsCl_6 at the X point. RIXS spectra at $\mathbf{q} = (5\ 5\ 6)$ and $(7\ 7\ 6)$ reveal four peaks at 0.3, 0.6, 1.3, and 2.1 eV with little temperature dependence. For clarity, the data are plotted with an offset. The inset highlights the $^1A_1$ peak at 2.1 eV which is suppressed for a scattering angle $2\theta = 90°$ (see main text).

C. Intra-t_{2g} excitations of K_2OsCl_6 in RIXS

High-resolution RIXS spectra of the intra-t_{2g} excitations reveal four peaks at about 0.3, 0.6, 1.3, and 2.1 eV (see Fig. 4). The local, on-site character of these excitations is highlighted by the insensitivity of the peak energies to the transferred momentum $\mathbf{q}$, i.e., the absence of a measurable dispersion (see Fig. 5). For a first assignment, we neglect spin-orbit coupling, $\zeta = 0$, and assume $10Dq = \infty$ for the cubic crystal-field splitting. In this case, the effect of the e_g orbitals on the intra-t_{2g} excitations vanishes. In a d^4 configuration there are 15 t_{2g}^4 states. Interorbital Coulomb interactions lift their degeneracy and yield a ninefold degenerate $^3T_1$ ground state and the $^1T_2$, ^1E, and $^1A_1$ excited states. The latter is expected at $5J_H$, while $^1T_2$ and ^1E show an energy of $2J_H$ [26,45]. Note, however, that these values correspond to a t_{2g}-only scenario, i.e., $10Dq = $
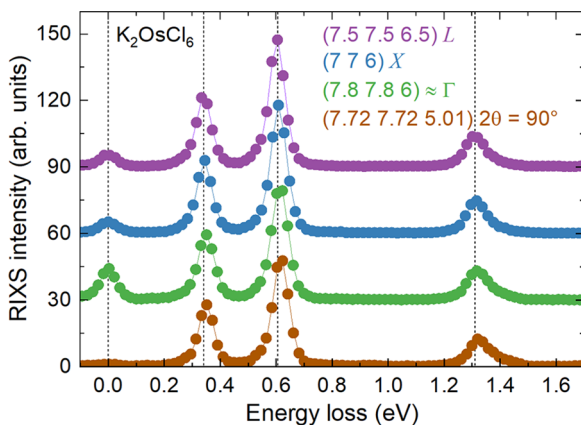
FIG. 5. Low-energy RIXS features in K_2OsCl_6 at 20 K at L, at X, and close to Γ. The latter data were measured in the vicinity of Γ to avoid the strong contribution of Bragg scattering right at Γ. Dashed lines indicate peak positions at X. The dispersion is negligible, highlighting the local character of the intra-t_{2g} excitations. Additionally, data at $(7.72\ 7.72\ 5.01)$ demonstrate the suppression of elastic Thomson scattering for $2\theta = 90°$.

∞; they are not suitable to estimate J_H for realistic values of $10Dq$ and ζ, as discussed below. The low-energy RIXS peaks at 0.3 and 0.6 eV reflect the effect of spin-orbit coupling, which splits the $^3T_1$ multiplet into the $J = 0$ ground state with Γ_1 symmetry and two excited states of $J = 1$ (Γ_4) and $J = 2$ ($\Gamma_3 + \Gamma_5$) character, respectively. The two contributions to the $J = 2$ peak at about 0.6 eV are expected to split in energy for finite values of the cubic crystal-field splitting $10Dq$. The fact that our RIXS data still show a single peak (see Fig. 5) indicates that the splitting is much smaller than the energy resolution $\delta E = 63$ meV. A finite Coulomb-induced splitting of the $J = 2$ states is most relevant in cubic $5d^2$ compounds. In these electron analogs of the two-t_{2g}-hole $5d^4$ configuration, the $J = 2$ multiplet has the lowest energy and its splitting for finite $10Dq$ determines the local ground state, which may lead to exotic multipolar phases [77–82]. For both $5d^4$ and $5d^2$, also the degeneracy of the $^1T_2$ and ^1E multiplets is lifted for finite $10Dq$. The asymmetric line shape of the RIXS peak around 1.3 eV at 20 and 300 K (see Fig. 4) indeed indicates a finite splitting between the cubic multiplets with a weaker feature on the high-energy side, as discussed in K_2RuCl_6 and Ba_2YIrO_6 [34,36].

Overall, the excitation spectrum agrees with previous RIXS results on $5d^4$ iridates [35–38]. RIXS data of $Yb_2Os_2O_7$ [43] also show the two low-energy modes below 1 eV but the intra-t_{2g} features at higher energies are hidden by a broad band that has been attributed to defects. Furthermore, the energy of the lowest excitation is much smaller in $Yb_2Os_2O_7$ due to a trigonal distortion [43]. In $4d^4$ K_2RuCl_6, the equivalent of the lower three features has been observed [34]. The $^1A_1$ peak at 2.1 eV thus far was only observed as a very weak feature in Sr_2YIrO_6 [35]. Comparing two data sets measured at the equivalent X points $(5\ 5\ 6)$ and $(7\ 7\ 6)$ (see Fig. 4), we find that the $^1A_1$ peak is suppressed in the latter, which has been recorded with a scattering angle 2θ close to $90°$. This geometry typically is chosen to suppress elastic Thomson scattering, explaining the absence of this peak in previous measurements on $5d^4$ compounds. An example for the successful suppression of the elastic line for $2\theta = 90°$ is given by the data for $(7.72\ 7.72\ 5.01)$ in Fig. 5. In contrast, the data for $(5\ 5\ 6)$ were measured with $2\theta = 66°$ and accordingly show a more pronounced elastic line. For $2\theta = 90°$, the polarization of the scattered light is perpendicular to the incident π polarization. This suggests that the $^1A_1$ feature is observable only for parallel polarization, which is supported by simulations using QUANTY [64,65].

Our peak assignment assumes cubic symmetry and neglects the phase transition from cubic to tetragonal symmetry at 45 K. However, the RIXS data measured at 20 and 300 K fully agree with each other (see Fig. 4), suggesting that the noncubic splitting is much smaller than the energy resolution $\delta E = 63$ meV. This is supported by the infrared data, which were measured with $\delta E = 0.25$ meV. A thorough analysis of the temperature dependence of the infrared data reveals a noncubic splitting of about 4 meV, as discussed below.

D. Optical conductivity of K_2OsCl_6

Based on the different selection rules, optical spectroscopy and RIXS are complementary techniques. The optical conduc-
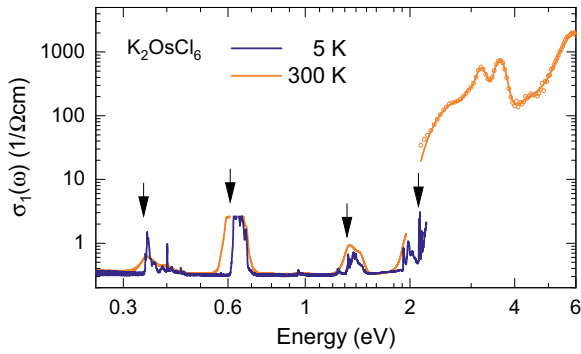
FIG. 6. Optical conductivity $\sigma_1(\omega)$ of K_2OsCl_6. Note the logarithmic scales. The strong absorption features above the Mott gap at 2.2 eV have been measured by ellipsometry, while the data in the transparent range below the gap with much smaller values of $\sigma_1(\omega)$ are based on the transmittance $T(\omega)$. The latter is suppressed below the noise level above 2.2 eV and around 0.6 eV, limiting the maximum value of $\sigma_1(\omega)$ that can be determined via $T(\omega)$ for the given sample thickness. Below the Mott gap, $\sigma_1(\omega)$ shows (phonon-assisted) intra-t_{2g} excitations in agreement with RIXS (arrows depict the RIXS intra-t_{2g} peak energies). Additionally, $\sigma_1(\omega)$ at 5 K reveals an exciton around 2.0 eV and two tiny features at about 0.95 and 1.25 eV that can be assigned to intersite overtones of the low-energy intra-t_{2g} excitations. For the ellipsometry data, symbols depict the result obtained from direct inversion of the raw data, while the solid line shows a fit of the raw data that additionally takes into account the low values of σ_1 below 2 eV. Around the gap, in the transition range from weak to strong absorption, the fit yields a very reasonable estimate of $\sigma_1(\omega)$.

tivity $\sigma_1(\omega)$ is dominated by electric dipole active transitions. Considering the orbital and electronic excitations in a Mott insulator, the dominant absorption features arise from *intersite* processes such as excitations across the Mott gap, in our case $|d_i^4 d_j^4\rangle \rightarrow |d_i^3 d_j^5\rangle$, or charge-transfer excitations $|5d_{Os}^4 3p_{Cl}^6\rangle \rightarrow |5d_{Os}^5 3p_{Cl}^5\rangle$. In Fig. 6, the Mott gap corresponds to the steep rise of $\sigma_1(\omega)$ above 2.2 eV. In contrast, RIXS at the Os L edge is dominated by on-site excitations [35–37,43,49], as discussed above, in particular for incident energies tuned to t_{2g} resonance. In the presence of inversion symmetry, on-site crystal-field excitations such as the intra-t_{2g} excitations are parity forbidden in $\sigma_1(\omega)$ but can become weakly allowed for instance in a phonon-assisted process. The corresponding spectral weight is several orders of magnitude smaller. Such weak features can only be studied for energies below the Mott gap where they are not hidden by stronger absorption processes (see Fig. 6).

1. Intersite excitations in $\sigma_1(\omega)$

Concerning the strong absorption features in $\sigma_1(\omega)$ above the Mott gap, we have to distinguish charge-transfer excitations between Cl and Os states from Mott-Hubbard excitations between Os states on different sites. One expects a larger spectral weight for the charge-transfer excitations due to the larger hopping matrix elements between Cl $3p$ and Os $5d$ states compared to Os intersite hopping. Accordingly, the strongest peak at about 6 eV can be assigned to a charge-transfer excitation, in agreement with the RIXS feature at 5.7 eV. The three peaks

in $\sigma_1(\omega)$ between 2 and 4 eV correspond to Mott-Hubbard excitations involving t_{2g} states, $|t_{2g_i}^4 t_{2g_j}^4\rangle \rightarrow |t_{2g_i}^3 t_{2g_j}^5\rangle$. Their energy mainly reflects the on-site Coulomb repulsion U, while the splitting is caused by J_H and ζ. In $4d^4$ Ca_2RuO_4, the relative spectral weight of these bands has been employed to estimate ζ [33]. Comparing $\sigma_1(\omega)$ with the RIXS data, we emphasize that the origin of the RIXS features between 2 and 4 eV is very different. RIXS shows on-site excitations to e_g states, as demonstrated by the resonance behavior. The pronounced difference between the two techniques is based on the on-site energy U that has to be paid in the optical Mott-Hubbard excitations. In $\sigma_1(\omega)$, Mott-Hubbard excitations to e_g states $|t_{2g_i}^4 t_{2g_j}^4\rangle \rightarrow |t_{2g_i}^3 (t_{2g}^4 e_g^1)_j\rangle$ are expected to occur roughly $10Dq$ higher in energy than the corresponding t_{2g} bands, i.e., above about 6 eV. In K_2OsCl_6, these processes hence overlap with the charge-transfer excitations discussed above.

The onset of excitations across the Mott gap can be determined very well from the transmittance $T(\omega)$ which is strongly suppressed by the steep increase of absorption. This limits the accessible frequency window in our measurement on a single crystal with thickness $d = 120$ μm (see Fig. 6). At 5 K, the onset is at $\Delta = 2.2$ eV. With increasing temperature, the onset shifts to lower energy, roughly to 1.9 eV at 300 K, while the slope of the steep increase in $\sigma_1(\omega)$ is reduced [see Fig. 7(a)]. The change of slope shows that the main origin of this shift is not a possible small temperature dependence of the gap itself. The enhanced absorption below 2.2 eV predominantly can be attributed to thermally activated phonon-assisted excitations across the gap, i.e., the Urbach tail.

Below the Mott gap, the optical data show three additional absorption bands that are absent in the RIXS data. The strongest one is observed between 1.9 and 2.1 eV, which is very close to the Mott gap [see Fig. 7(a)]. This feature is well separated from the $^1A_1$ intra-t_{2g} excitation at 2.117 eV. Its spectral weight is comparable to the weak intra-t_{2g} excitations but the absence of a corresponding RIXS feature strongly points to a different origin. We therefore assign it to an exciton with $5d^3$ and $5d^5$ configurations on neighboring Os sites. This exciton is stabilized by nearest-neighbor Coulomb attraction and may induce a local relaxation of the Cl_6 octahedra. In this case, the substructure of this absorption feature tentatively can be attributed to phonon sidebands. The exciton scenario is strongly supported by the data of K_2OsBr_6, in which both the Mott gap and the excitonic absorption feature are shifted to lower energy by about 0.3–0.4 eV [see Fig. 7(b)]. In contrast, the intra-t_{2g} excitation energies are very similar in K_2OsBr_6 and K_2OsCl_6, as discussed in Sec. VI.

The two other below-gap absorption bands without a counterpart in RIXS are the two tiny features in $\sigma_1(\omega)$ at about 0.95 and 1.25 eV (see Fig. 6). We attribute also these bands to intersite excitations. They can be explained as a combination and overtone of the intra-t_{2g} excitations at about 0.35 and 0.65 eV, i.e., the simultaneous excitation of intra-t_{2g} excitations on two neighboring Os sites. In the honeycomb compound $\alpha - RuCl_3$ it has been shown that such double or even triple excitations may carry sizable spectral weight [58].
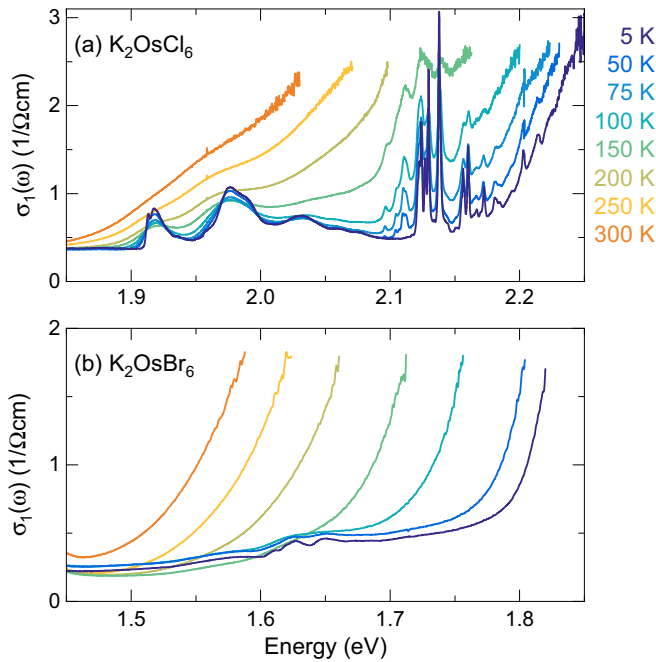
FIG. 7. Temperature dependence of $\sigma_1(\omega)$ close to the Mott gap in (a) K_2OsCl_6 and (b) K_2OsBr_6. In K_2OsCl_6, the onset of excitations across the Mott gap is observed at 2.2 eV at 5 K. This onset is washed out with increasing temperature since additional processes with simultaneous annihilation of thermally excited phonons reduce the total excitation energy in the Urbach tail. The $^1A_1$ intra-t_{2g} excitation is observed at 2.117 eV, and the many narrow lines around it correspond to phonon sidebands. In contrast to the $^1A_1$ peak, the absorption band between 1.9 and 2.1 eV has no counterpart in RIXS and can be assigned to an exciton. For comparison, the data of K_2OsBr_6 show the Mott gap at 1.8 eV at 5 K and a very similar temperature dependence. In K_2OsBr_6, the exciton is observed around 1.6–1.7 eV.

Due to interaction effects, the peak energies do not have to perfectly match the simple sum of the individual excitation energies.

2. Intra-t_{2g} excitations in $\sigma_1(\omega)$

Considering the intra-t_{2g} excitations (see Figs. 4 and 8), the optical data show a rich structure where RIXS finds a single peak. Apart from the very different energy resolution, the selection rules and hence the excitation mechanisms are different. K_2OsCl_6 shows inversion symmetry, therefore the electric dipole matrix element for a local, even-parity $d - d$ excitation vanishes. Finite spectral weight appears in $\sigma_1(\omega)$ based on either a phonon-assisted process, or in the magnetic dipole channel, or due to electric quadrupolar or higher-order moments. We exemplify this by the data on the $^1A_1$ multiplet [see Fig. 8(d)].

At 5 K, we find a tiny zero-phonon magnetic-dipole mode at $E_{^1A_1} = 2117$ meV. This assignment is based on the temperature dependence of the phonon-assisted electric dipole features observed at $E_{^1A_1} \pm E_{ph}$. At 5 K, we only find modes at $E_{^1A_1} + E_{ph}$ for different symmetry-breaking phonons with, e.g., $E_{ph} = 7$, 13, or 21 meV, as indicated in Fig. 8(d) by
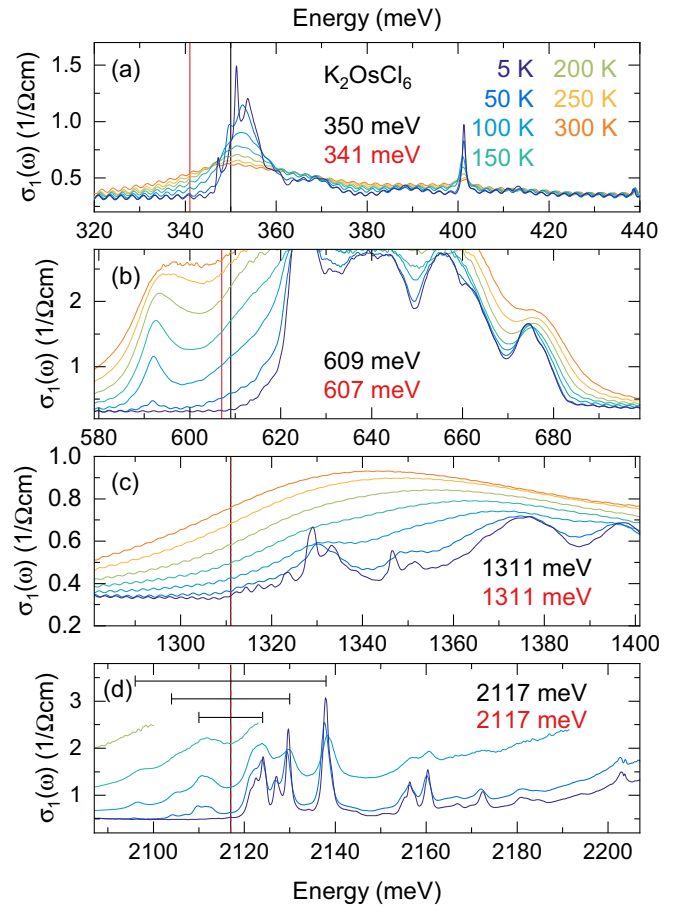
FIG. 8. Intra-t_{2g} excitations of K_2OsCl_6 in $\sigma_1(\omega)$. The panels depict excitations from $J = 0$ to (a) $J = 1$, i.e., Γ_1 to Γ_4; (b) the split $J = 2$ states, i.e., Γ_1 to Γ_5 and Γ_3; (c) the split $^1T_2$ and ^1E states; and (d) $^1A_1$. Each panel covers a window of the same width, 120 meV. In each panel, the vertical black line denotes the bare electronic (zero-phonon) energy, while the red line shows the fit result of the RIXS data. In $\sigma_1(\omega)$, the spectral weight is dominated by phonon sidebands. In (b), the transmittance around the peak maximum is suppressed below the noise level, which limits the measurable range of $\sigma_1(\omega)$. In (d), the horizontal black lines denote phonon sidebands at $E_{^1A_1} \pm E_{ph}$ with $E_{ph} = 7$, 13, and 21 meV. The small periodic wiggles, most pronounced at lower frequency, i.e., panel (a), are caused by Fabry-Pérot interference fringes in the transmittance. In $\sigma_1(\omega)$, they are an artifact of our analysis and have to be ignored.

the right ends of the horizontal black lines. With increasing temperature, these phonon modes become thermally populated and the corresponding phonon-annihilation features appear at $E_{^1A_1} - E_{ph}$, strongly supporting our assignment. The spectral weight of the phonon-annihilation peaks is governed by the Boltzmann factor. Hence peaks at lower energy $E_{^1A_1} - E_{ph}$ with larger E_{ph} become noticeable at higher temperature. Further features above 2150 meV correspond to a progression of phonon sidebands in a vibronic Franck-Condon picture [52,54]. Typically, this rich phonon-related pattern of crystal-field excitations can be resolved in measurements of transition-metal ions substituted into a host crystal [60]. In single crystals, this pattern usually is washed out. Exceptions have been observed in quasimolecular crystals such
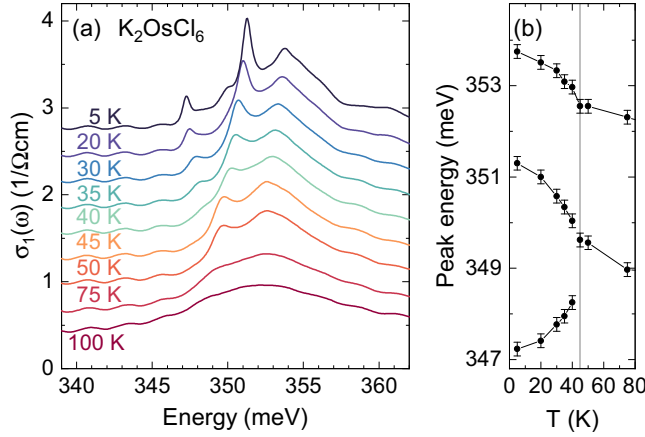
FIG. 9. Temperature dependence of $\sigma_1(\omega)$ in K_2OsCl_6 across the structural phase transition at 45 K. (a) Excitations to $J = 1$ [see Fig. 8(a)]. Data have been offset for clarity. (b) Corresponding peak energies as a function of temperature. Below 45 K, the peak splitting of the mode at $E_0 \approx 349$ meV reflects the noncubic crystal field. The feature at 352–354 meV is a phonon sideband that is present already in the cubic phase.

FIG. 10. Energies of on-site $d - d$ excitations for a $5d^4$ configuration in a cubic crystal field. Left: First switching on $10Dq$ separates the t_{2g}^4 states at zero energy from $t_{2g}^3 e_g^1$ states and states with more than one electron in the e_g orbitals. Middle left: Effect of J_H for $10Dq = 3.3$ eV and $\zeta = 0$. Here, the $^3T_1$ multiplet forms the ground state. Middle right: Spin-orbit coupling ζ yields a $J = 0$ ground state and four groups of intra-t_{2g} excitations. Red circles denote the experimental energies of K_2OsCl_6 used to determine the electronic parameters. Right: Effect of a reduction of $10Dq$ for finite J_H and ζ, mimicking the trend from K_2OsCl_6 to K_2OsBr_6.

as K_3NiO_2 with isolated NiO_2 units [53], and the rich optical spectra of K_2OsCl_6 most probably reflect the weak interactions between well-separated $OsCl_6$ octahedra. A detailed assignment of the sidebands in K_2OsCl_6 has been discussed previously [60].

Similar to the analysis of the $^1A_1$ peak, we use the optical data to find the bare electronic excitation energies of the intra-t_{2g} excitations at 350, 609, and 1311 meV. The value 350 meV corresponds to the energy of a feature that can be assigned to a magnetic-dipole transition from $J = 0$ to 1, i.e., Γ_1 to Γ_4 [83]. This peak splits below 45 K (see Fig. 9 and discussion below), but for comparison with theory, we employ the value at 50 K in the cubic phase. The two further energies 609 and 1311 meV are deduced from the temperature dependence of those absorption bands in $\sigma_1(\omega)$, in agreement with Ref. [60].

To compare the excitation energies found in RIXS and optics, we extract the RIXS peak energies for the intra-t_{2g} excitations from a fit that uses a series of Voigt profiles. We anchor the RIXS energy scale via the optical result of 2117 meV for the highest intra-t_{2g} excitation energy, as mentioned in Sec. IV. For the other low-energy RIXS peaks, this yields 341(1), 607(1), 1311(9), and 1373(140) meV, where the values in parentheses state the error bar of the fit. Remarkably, the first three values agree with the optical data within less than 10 meV (see Fig. 8). This excellent result once more corroborates the local character of these excitations. For the small shoulder around 1.37 eV, the uncertainty of the peak energy is much larger. We hence neglect this value for the further analysis.

The effect of the structural phase transition at 45 K is addressed in Fig. 9. In the antifluorite halides, a noncubic crystal-field splitting Δ_{CF} is driven by tilts and rotary or librational modes of the metal-ligand octahedra [84–87]. In $\sigma_1(\omega)$, an intra-t_{2g} excitation at E_0 gives rise to phonon-assisted peaks at $E_0 + E_{ph}$ already in the cubic phase, as discussed above

for the $^1A_1$ mode. For the absorption band around 350 meV, we find a magnetic-dipole excitation at $E_0 \approx 349$ meV [83] and a phonon sideband at 352 meV, both at 50 and 75 K in the cubic phase. However, the peak at E_0 exhibits a noncubic peak splitting below 45 K. At 5 K, we observe peaks at $E_{0,a} = 347$ meV and $E_{0,b} = 351$ meV, i.e., $\Delta_{exp} \approx 4$ meV. This splitting scenario is supported by the temperature dependence. With decreasing temperature, $E_{0,a}$ decreases whereas the upper two peak energies $E_{0,b}$ and $E_{0,b} + E_{ph}$ show a common increase [see Fig. 9(b)]. Further support stems from the small shoulder observed at $E_{0,a} + E_{ph} = 350$ meV at 5 K [see Fig. 9(a)]. A similar behavior is observed for the $^1T_2$ excitation at 1.3 eV (not shown). This peak splitting $\Delta_{exp} \approx 4$ meV of the $J = 1$ band sets the energy scale of Δ_{CF} of K_2OsCl_6. For instance for a small tetragonal field $|\Delta_{CF}| \ll \zeta$, one finds $|\Delta_{CF}| \approx 2\Delta_{exp}$ [33].

E. Calculation of energy levels of K_2OsCl_6

For the analysis of the electronic parameters, we stick to cubic symmetry. In a single-site model, the relevant parameters for the energy levels are the cubic crystal-field splitting $10Dq$ between t_{2g} and e_g levels, spin-orbit coupling ζ, and the Coulomb interaction within the $5d$ shell. In spherical approximation, the latter can be described by the Slater integrals F^2 and F^4, which are used to calculate Hund's coupling $J_H = 1/14 (F^2 + F^4)$ within the entire $5d$ shell [45]. Note that F^0, equivalent to Hubbard U, does not contribute to the energy splitting for a single site with a fixed number of electrons. We calculate the multiplet energies using QUANTY [64,65]. Figure 10 displays the behavior as a function of $10Dq$, J_H, and ζ. Starting with $J_H = \zeta = 0$, the cubic crystal field yields a t_{2g}^4 ground state and raises the excitation energies of the $t_{2g}^{4-n} e_g^n$ states with $n = 1$ to 4 electrons in the e_g subshell.
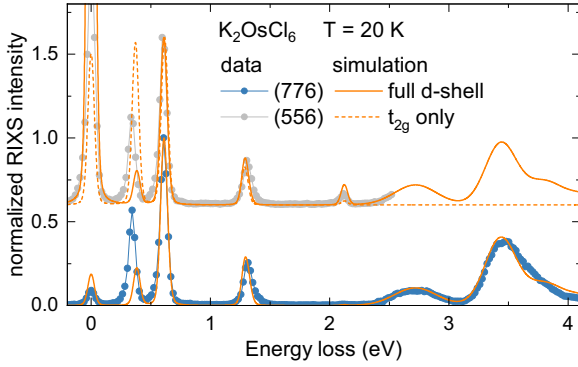
FIG. 11. Measured and calculated RIXS spectra of K_2OsCl_6. Solid orange lines: Simulation based on the fit result for the full d-shell model (see Table I). To account for the polarization dependence of the $^1A_1$ transition at 2.1 eV, we consider two different values of **q**. Dashed: Corresponding result of the Kanamori model for $J_H^{eff} = 0.28$ eV and $\zeta^{eff} = 0.41$ eV. Peak widths are adapted to the data. Offsets have been used for clarity.

Switching on J_H splits each of these five branches. We focus on the 15 t_{2g}^4 states. These are split into the $^3T_1$ ground state and the $^1T_2$, ^1E, and $^1A_1$ excited states. The excitation energies of roughly $3/2\,J_H$ and $4\,J_H$ are approximately 20–25% lower than for $10Dq = \infty$, reflecting a small but finite admixture of e_g character. Finally, spin-orbit coupling ζ causes a further fanning out of the energies and splits the $^3T_1$ ground state into three branches. In the limit of $10Dq = J_H = \infty$ these correspond to the eigenstates $J = 0$, 1, and 2. The intra-t_{2g} excitations within the t_{2g}^4 states form four groups of excitations that cover the range up to about 2 eV. The lowest $t_{2g}^3e_g^1$ level corresponds to the high-spin ^5E state with $S = 2$. With all four spins being parallel, it is strongly favored by J_H. Even though the ^5E state is well separated from other levels (see Fig. 10), the width of this t_{2g}-to-e_g excitation is much larger than observed for the intra-t_{2g} peaks (see Fig. 11). This suggests a finite mixing with excitations across the Mott gap at 2.2 eV.

Optical studies of Os^{4+} impurities in different host crystals have reported different sets of electronic parameters [88–91]. Also for optical data on single crystals of K_2OsCl_6, it has

been found that the determination of the electronic parameters is difficult [60], foremost because the crystal-field splitting $10Dq$ is hard to obtain from the optical data. The combined approach of RIXS and optics is pivotal here to resolve these ambiguities.

To determine the parameters of the d-shell model for K_2OsCl_6, we consider the four energies of the intra-t_{2g} excitations from the optical data and the $t_{2g}^3e_g^1$ excitations observed at 2.72 and 3.43 eV in RIXS (see red circles in Fig. 10). We neglect peaks at higher energies where an unambiguous assignment is hindered by the large number of similar excitation energies. In the fit, we minimize the absolute difference between experimental peak energies and calculated ones. This yields the parameters $10Dq = 3.3$ eV, $\zeta = 0.34$ eV, $F^2 = 3.7$ eV, and $F^4 = 2.2$ eV, resulting in $J_H = 0.43$ eV. Note that the value of $10Dq$ agrees very well with our simple estimate discussed above. Figure 11 compares the calculated result for direct L_3-edge RIXS [49] for this parameter set with the experimental data. Overall, the peak energies as well as the relative peak intensities are well described. Calculations using density functional theory find $10Dq = 3$ eV and $\zeta = 0.4$ eV for K_2OsCl_6 [63], in reasonable agreement with our results.

The calculated excitation energies are given in Table I. For the splittings of the excitations at about 0.6 and 1.3 eV, the model predicts values of 20–35 meV in cubic symmetry, which is well below the RIXS resolution limit and agrees with the energy scale observed in the optical data. Concerning the fitted energies, the deviations are less than 7 meV for four of the six energies, an excellent result. Upon a closer look, the largest deviation of 33 meV is found for the peak lowest in energy, and the intensity of this feature is underestimated. A similar observation has been reported for 4d^4 K_2RuCl_6, where it has been discussed in terms of a possible role of vibronic coupling, i.e., a dynamic Jahn-Teller splitting of the excited $J = 1$ triplet state [34,44]. For K_2OsCl_6, our optical data resolve the vibronic sidebands in the excited states (see Fig. 8), but do not hint at a particular importance of vibronic effects for the feature around 0.35 eV. We find, however, that a small change in the parameters can eliminate this apparent shortcoming of the model. In a second fit, we minimize the *relative* energy difference between experiment and model. This results in the very similar parameter set $10Dq = 3.4$ eV,

TABLE I. Experimental and calculated excitation energies. The four intra-t_{2g} energies are taken from the optical data; the two e_g levels above 2.7 eV come from RIXS. Dashes denote peaks that are not resolved in the experiment. For K_2OsCl_6 (K_2OsBr_6), the parameters of the d-shell model are $10Dq = 3.27$ eV (2.85 eV), $\zeta = 0.336$ eV (0.325 eV), $F^2 = 3.73$ eV (3.90 eV), and $F^4 = 2.22$ eV (2.01 eV), which corresponds to $J_H = 0.425$ eV (0.422 eV).

Multiplet	Expt. Cl (meV)	Fit Cl (meV)	Expt. Br (meV)	Fit Br (meV)
$\Gamma_4(^3T_1)$	350	383	349	388
$\Gamma_5(^3T_1)$	609	608	604	604
$\Gamma_3(^3T_1)$	–	631	–	632
$^1T_2$	1311	1289	1285	1267
^1E	–	1323	–	1312
$^1A_1$	2117	2123	–	2050
^5E	2721	2716	2391	2381
^3E	3428	3432	3033	3042

$\zeta = 0.34$ eV, and $J_H = 0.42$ eV and yields the energies 358, 600, 1278, and 2139 meV for the four lowest excitations. For all four, the relative difference is less than 2.6%, a very reasonable result. In terms of absolute energy differences, the deviation between fit and experiment is reduced to 8 meV for the peak at 350 meV while the description of the other peaks is slightly worse compared to the first fit. Finally, we have checked that inclusion of the Cl $3p$ orbitals and ligand-to-metal charge-transfer processes [64] yields very similar results. Overall, we find $J_H/\zeta \approx 1.3$ which puts K$_2$OsCl$_6$ in the intermediate regime between *LS* coupling with $J_H/\zeta \to \infty$ and jj coupling for $J_H/\zeta \to 0$.

F. Parameters in the Kanamori model

Thus far we discussed a model that takes the entire d shell into account. In contrast, the related $5d^4$ iridate data in Refs. [35–38] were analyzed using the Kanamori model that assumes $10Dq = \infty$, i.e., it considers only t_{2g} orbitals. For a comparison, it is important to quantify how the parameter values depend on the chosen model. In the Kanamori model, the only parameters are ζ^{eff} and $J_H^{\text{eff}} = 3/49\,F^2 + 20/441\,F^4$ [45]. With $10Dq = \infty$, the Kanamori model restores the degeneracy of $^1T_2$ and ^1E around 1.3 eV and of the Γ_3 and Γ_5 states of $J = 2$ around 0.6 eV, as mentioned in Sec. V C. Hence the model has only four intra-t_{2g} excitation energies. For simplicity, we call these energies $E(1)$ to $E(4)$, in ascending order. Simple expressions for $E(1)$ to $E(4)$ are given in Ref. [44].

A fit of the four intra-t_{2g} excitation energies with the t_{2g}-only Kanamori model yields $J_H^{\text{eff}} = 0.28$ eV and $\zeta^{\text{eff}} = 0.41$ eV and the energies 371, 616, 1288, and 2125 meV. A corresponding simulated RIXS spectrum is shown in Fig. 11. Similar to the result obtained for the full d shell, the relative deviation between fit and data is largest for the lowest mode. Again, a slightly different set of parameters yields excellent agreement for the lowest excitation energies. Choosing $J_H^{\text{eff}} = 310$ meV and $\zeta^{\text{eff}} = 399$ meV describes the lowest three peaks of K$_2$OsCl$_6$ within 1 meV and $E(4)$ within 6%. Overall, this suggests $J_H^{\text{eff}}/\zeta^{\text{eff}} \approx 3/4$.

Another possibility to determine this quantity is given by the ratio $E(2)/E(1)$, which varies from 3 for *LS* coupling to 1 for jj coupling [see Fig. 12(a)]. For K$_2$OsCl$_6$ with 609 meV/350 meV ≈ 1.7, this corroborates $J_H^{\text{eff}}/\zeta^{\text{eff}} \approx 3/4$. Remarkably, very similar values of the ratio $E(2)/E(1)$ have been reported for several $5d^4$ iridates [see Fig. 12(b)], highlighting the close relationship of the properties of this series of $5d^4$ compounds.

As long as the corresponding model is specified, both $J_H/\zeta \approx 1.3$ for the entire $5d$ shell and $J_H^{\text{eff}}/\zeta^{\text{eff}} \approx 3/4$ in the t_{2g}-only model are valid. For $J_H \approx \zeta$, the two models predict

$$E(J = 2) \approx \frac{3}{2}\zeta\left(1 + \frac{2\zeta}{10Dq}\right) \tag{2}$$

$$E(2) \approx \frac{3}{2}\zeta^{\text{eff}} \tag{3}$$

for the second excitation energy and hence $\zeta^{\text{eff}}/\zeta \approx 1.2$ in the $5d^4$ compounds. Additionally, the different definitions of Hund's coupling yield $J_H^{\text{eff}}/J_H \approx 0.77$. Concerning the
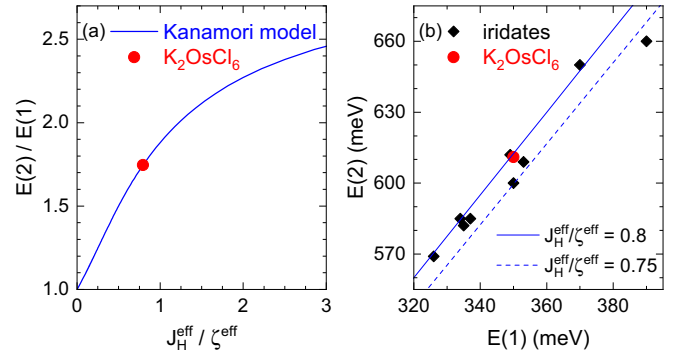
FIG. 12. Analysis based on the t_{2g}-only Kanamori model. (a) The ratio $E(2)/E(1)$ varies between 1 for $J_H^{\text{eff}}/\zeta^{\text{eff}} \to 0$ and 3 for $J_H^{\text{eff}}/\zeta^{\text{eff}} \to \infty$. For K$_2$OsCl$_6$, it yields $J_H^{\text{eff}}/\zeta^{\text{eff}} \approx 3/4$. (b) Comparison of the two lowest excitation energies in K$_2$OsCl$_6$ and related $5d^4$ iridates [35–38]. For all of them, $J_H^{\text{eff}}/\zeta^{\text{eff}}$ is very similar.

energies of the intra-t_{2g} excitations, the t_{2g}-only Kanamori model and the model for the full d shell work equally well. The main shortcoming of both models is the intensity of the lowest excitation, which is too small in the d-shell model but too large in the Kanamori model (see Fig. 11). This suggests that the intensity of the lowest RIXS peak depends sensitively on $10Dq$ and on the admixture of e_g character.

VI. RESULTS ON THE BROMIDES

RIXS spectra of K$_2$OsCl$_6$, K$_2$OsBr$_6$, and Rb$_2$OsBr$_6$ are compared in Fig. 13. We find a close resemblance of the RIXS data of K$_2$OsBr$_6$ and Rb$_2$OsBr$_6$, i.e., a very small effect of the A ion. Hence we focus on the comparison of K$_2$OsBr$_6$ and K$_2$OsCl$_6$. The behavior is different above and below 2 eV. In RIXS we find the intra-t_{2g} excitation energies of K$_2$OsBr$_6$ at 0.34, 0.60, and 1.27 eV. Compared to K$_2$OsCl$_6$, these are reduced by about 1, 2, and 3%, respectively, i.e., they are almost unaffected by the choice of the halide. In contrast, the peak energies associated to the e_g and charge-transfer excitations
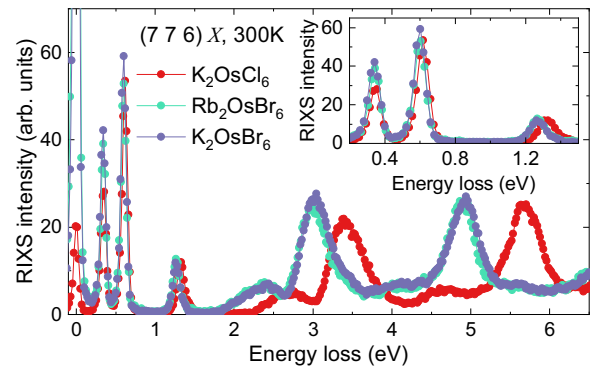
FIG. 13. Comparison of RIXS spectra of K$_2$OsCl$_6$, K$_2$OsBr$_6$, and Rb$_2$OsBr$_6$. The difference in size and electronegativity between Br and Cl ions alters the crystal-field and charge-transfer excitations. In comparison, the intra-t_{2g} peaks are less affected by the change of the ligand, as highlighted in the inset.
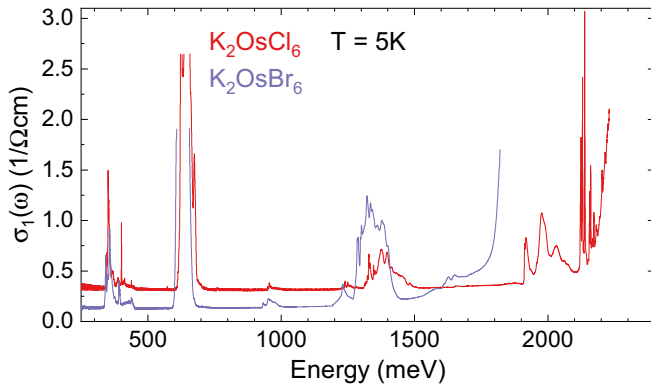
FIG. 14. Optical conductivity of K$_2$OsCl$_6$ and K$_2$OsBr$_6$. The main change is the shift of the Mott gap from 2.2 to 1.8 eV. The small offset in the K$_2$OsCl$_6$ data indicates a possible surface issue. Note that we polished this sample with CeO$_2$ in propanol, while the K$_2$OsBr$_6$ crystal was measured as grown.

are reduced by about 12–14% in K$_2$OsBr$_6$ with respect to the chloride. More precisely, the peak energies are 2.4 and 3.0 eV for the strongest $t_{2g}^3 e_g^1$ transitions and 4.0 and 4.9 eV for the charge-transfer excitations $|5d_{\text{Os}}^4 4p_{\text{Br}}^6\rangle \rightarrow |5d_{\text{Os}}^5 4p_{\text{Br}}^5\rangle$. The very similar intensity profile of the two compounds indicates that the main effect at high energy is captured by a renormalization of the energy scale, i.e., of $10Dq$ and Δ_{CT}. Both parameters are affected by the difference in ionic size and electronegativity. Empirically, the effect of different ligands on $10Dq$ is described by the spectrochemical series [53], and the reduction of Δ_{CT} from bromides to chlorides has been observed in other transition-metal compounds as well, both in optics and RIXS [92,93]. For 5d halides, a very similar shift has been reported from K$_2$IrCl$_6$ to K$_2$IrBr$_6$ [76].

In analogy to the discussion of K$_2$OsCl$_6$ above, we identify $\Delta_{\text{CT}}^{\text{Br}} = 4.0$ eV via the lowest charge-transfer excitation. Furthermore, a fit of the excitation energies using multiplet calculations yields the parameters $10Dq^{\text{Br}} = 2.9$ eV, $\zeta^{\text{Br}} = 0.33$ eV, and $J_H^{\text{Br}} = 0.42$ eV. Compared to K$_2$OsCl$_6$, the spin-orbit coupling constant is reduced by about 4 %, while the change of J_H is negligible (see Table I). These results are in good agreement with predictions of density functional theory for the reduction of $10Dq$, Δ_{CT}, and ζ from K$_2$OsCl$_6$ to K$_2$OsBr$_6$ [63]. A similar reduction of the spin-orbit coupling constant of about 5 % has been reported from K$_2$IrCl$_6$ to K$_2$IrBr$_6$ [76]. The effect of a reduction of $10Dq$ on the energy levels of the multiplet model is shown in the right panel of Fig. 10. While the $t_{2g}^3 e_g^1$ levels decrease linearly in energy, the t_{2g}^4 states hardly change. In general, lower values of $10Dq$ and Δ_{CT} indicate a stronger admixture of e_g and 4p ligand character into the t_{2g} states. This, in turn, reduces the effective value of ζ. However, the large ratio of $10Dq/\zeta \approx 10$ explains why the sizable reduction of $10Dq$ has only a small effect on ζ.

The optical conductivity $\sigma_1(\omega)$ of K$_2$OsBr$_6$ is depicted in Figs. 14 and 7(b). Note that the larger thickness $d^{\text{Br}} = 170 \,\mu$m of the bromide sample limits the accessible values of $\sigma_1(\omega)$ to below 2 $(\Omega\,\text{cm})^{-1}$, somewhat lower than in the thinner chloride sample. The most pronounced difference to

the data of K$_2$OsCl$_6$ is the value of the Mott gap, which is shifted down by about 0.4 eV to 1.8 eV at 5 K. This shift masks the $^1A_1$ excitation which occurs at 2.1 eV in K$_2$OsCl$_6$. Along with the Mott gap, also the excitation energy of the exciton is reduced, as already discussed in connection with Fig. 7. At lower energy, the small shifts of the intra-t_{2g} excitations of less than 1% for the lowest excitation and about 1–2 % for the bands at 0.6 and 1.3 eV agree with the RIXS results.

VII. CONCLUSION

In conclusion, we have probed the local electronic structure of the 5d^4 hexahalogenoosmates K$_2$OsCl$_6$, K$_2$OsBr$_6$, and Rb$_2$OsBr$_6$ with magnetic and spectroscopic methods. These measurements reveal nonmagnetic $J = 0$ behavior, as expected for a clean 5d^4 system in which both defects and exchange interactions are negligible. Combining RIXS and optical spectroscopy, we can assign the multiplet excitation energies with high accuracy and extract the electronic parameters by comparison with local multiplet calculations. RIXS at the transition-metal L edge is most sensitive to on-site $d - d$ excitations, which in the optical data give rise to weak, typically phonon-assisted features. For the antifluorite-type Os halides, a central advantage of RIXS is the ability to determine $10Dq$ via the observation of local excitations into the e_g subshell also above the Mott gap. Due to the weak interactions between OsX$_6$ (X = Cl, Br) octahedra, both the e_g excitations and the charge-transfer excitations are narrow and very well defined in RIXS. As a complementary technique, optical spectroscopy allows us to determine the small noncubic crystal-field splitting of 4 meV below 45 K in K$_2$OsCl$_6$. Furthermore, it is sensitive to intersite processes such as excitations across the Mott gap at 2.2 eV and reveals an exciton around 1.9–2.1 eV. These results establish the presented compounds as realizations of clean cubic $J = 0$ systems in the intermediate coupling regime with $J_H/\zeta \approx 1.3$ or $J_H^{\text{eff}}/\zeta^{\text{eff}} \approx 3/4$. Accordingly, Coulomb interaction and spin-orbit coupling have to be taken on equal footing. This value of $J_H^{\text{eff}}/\zeta^{\text{eff}}$ is very similar to results reported for 5d^4 iridates [35–38], highlighting the close relationship between these compounds. The comparison of the data from chloride and bromide samples shows a 20% decrease of the Mott gap as well as a reduction of about 12–14% of $10Dq$ and of the charge-transfer energy Δ_{CT}, in agreement with predictions of density functional theory [63]. Due to the large size of $10Dq$ and Δ_{CT} with respect to J_H and ζ, this sizable change has only a marginal effect on intra-t_{2g} energies, which are reduced by 1–3%. In contrast to previous studies on 5d^4 $J = 0$ compounds, where the determination of ζ and J_H has turned out to be difficult, we find that both chloride and bromide samples are well described by $\zeta = 0.33$–0.34 eV and $J_H = 0.42$–0.43 eV. These values may serve as a solid reference for future studies on Os compounds.

[1] W. Witczak-Krempa, G. Chen, Y. B. Kim, and L. Balents, Correlated quantum phenomena in the strong spin-orbit regime, Annu. Rev. Condens. Matter Phys. **5**, 57 (2014).

[2] J. G. Rau, E. K.-H. Lee, and H.-Y. Kee, Spin-orbit physics giving rise to novel phases in correlated systems: Iridates and related materials, Annu. Rev. Condens. Matter Phys. **7**, 195 (2016).

[3] R. Schaffer, E. K.-H. Lee, B.-J. Yang, and Y. B. Kim, Recent progress on correlated electron systems with strong spin-orbit coupling, Rep. Prog. Phys. **79**, 094504 (2016).

[4] T. Takayama, J. Chaloupka, A. Smerald, G. Khaliullin, and H. Takagi, Spin-orbit-entangled electronic phases in $4d$ and $5d$ transition-metal compounds, J. Phys. Soc. Jpn. **90**, 062001 (2021).

[5] D. I. Khomskii and S. V. Streltsov, Orbital effects in solids: Basics, recent progress, and opportunities, Chem. Rev. **121**, 2992 (2021).

[6] S. M. Winter, A. A. Tsirlin, M. Daghofer, J. van den Brink, Y. Singh, P. Gegenwart, and R. Valentí, Models and materials for generalized Kitaev magnetism, J. Phys.: Condens. Matter **29**, 493002 (2017).

[7] G. Cao and P. Schlottmann, The challenge of spin-orbit-tuned ground states in iridates, Rep. Prog. Phys. **81**, 042502 (2018).

[8] S. Trebst and C. Hickey, Kitaev materials, Phys. Rep. **950**, 1 (2022).

[9] G. Jackeli and G. Khaliullin, Mott Insulators in the Strong Spin-Orbit Coupling Limit: From Heisenberg to a Quantum Compass and Kitaev Models, Phys. Rev. Lett. **102**, 017205 (2009).

[10] M. Hermanns, I. Kimchi, and J. Knolle, Physics of the Kitaev model: Fractionalization, dynamic correlations, and material connections, Annu. Rev. Condens. Matter Phys. **9**, 17 (2018).

[11] H. Takagi, T. Takayama, G. Jackeli, G. Khaliullin and S. E. Nagler, Concept and realization of Kitaev quantum spin liquids, Nat. Rev. Phys. **1**, 264 (2019).

[12] Y. Motome and J. Nasu, Hunting Majorana fermions in Kitaev magnets, J. Phys. Soc. Jpn. **89**, 012002 (2020).

[13] S. H. Chun, J.-W. Kim, J. Kim, H. Zheng, C. C. Stoumpos, C. D. Malliakas, J. F. Mitchell, K. Mehlawat, Y. Singh, Y. Choi, T. Gog, A. Al-Zein, M. Moretti Sala, M. Krisch, J. Chaloupka, G. Jackeli, G. Khaliullin, and B. J. Kim, Direct evidence for dominant bond-directional interactions in a honeycomb lattice iridate Na_2IrO_3, Nat. Phys. **11**, 462 (2015).

[14] M. Magnaterra, K. Hopfer, Ch. J. Sahle, M. Moretti Sala, G. Monaco, J. Attig, C. Hickey, I.-M. Pietsch, F. Breitner, P. Gegenwart, M. H. Upton, Jungho Kim, S. Trebst, P. H. M. van Loosdrecht, J. van den Brink, and M. Grüninger, RIXS observation of bond-directional nearest-neighbor excitations in the Kitaev material Na_2IrO_3, arXiv:2301.08340

[15] A. Revelli, C. C. Loo, D. Kiese, P. Becker, T. Fröhlich, T. Lorenz, M. Moretti Sala, G. Monaco, F. L. Buessen, J. Attig, M. Hermanns, S. V. Streltsov, D. I. Khomskii, J. van den Brink, M. Braden, P. H. M. van Loosdrecht, S. Trebst, A. Paramekanti, and M. Grüninger, Spin-orbit entangled $j = 1/2$ moments in Ba_2CeIrO_6: A frustrated fcc quantum magnet, Phys. Rev. B **100**, 085139 (2019).

[16] A. Revelli, M. Moretti Sala, G. Monaco, P. Becker, L. Bohatý, M. Hermanns, T. C. Koethe, T. Fröhlich, P. Warzanowski, T. Lorenz, S. V. Streltsov, P. H. M. van Loosdrecht, D. I. Khomskii, J. van den Brink, and M. Grüninger, Resonant inelastic x-ray incarnation of Young's double-slit experiment, Sci. Adv. **5**, eaav4020 (2019).

[17] A. Revelli, M. Moretti Sala, G. Monaco, M. Magnaterra, J. Attig, L. Peterlini, T. Dey, A. A. Tsirlin, P. Gegenwart, T. Fröhlich, M. Braden, C. Grams, J. Hemberger, P. Becker, P. H. M. van Loosdrecht, D. I. Khomskii, J. van den Brink, M. Hermanns, and M. Grüninger, Quasimolecular electronic structure of the spin-liquid candidate $Ba_3InIr_2O_9$, Phys. Rev. B **106**, 155107 (2022).

[18] G. Khaliullin, Excitonic Magnetism in Van Vleck–type d^4 Mott Insulators, Phys. Rev. Lett. **111**, 197201 (2013).

[19] O. N. Meetei, W. S. Cole, M. Randeria, and N. Trivedi, Novel magnetic state in d^4 Mott insulators, Phys. Rev. B **91**, 054412 (2015).

[20] D. I. Khomskii, *Transition Metal Compounds* (Cambridge University, New York, 2014).

[21] A. Akbari and G. Khaliullin, Magnetic excitations in spin-orbit coupled d^4 Mott insulator on square lattice, Phys. Rev. B **90**, 035137 (2014).

[22] N. Kaushal, J. Herbrych, G. Alvarez, and E. Dagotto, Magnetization dynamics fingerprints of an excitonic condensate t_{2g}^4 magnet, Phys. Rev. B **104**, 235135 (2021).

[23] A. Jain, M. Krautloher, J. Porras, G. H. Ryu, D. P. Chen, D. L. Abernathy, J. T. Park, A. Ivanov, J. Chaloupka, G. Khaliullin, B. Keimer, and B. J. Kim, Higgs mode and its decay in a two-dimensional antiferromagnet, Nat. Phys. **13**, 633 (2017).

[24] S. Kunkemöller, D. Khomskii, P. Steffens, A. Piovano, A. A. Nugroho, and M. Braden, Highly Anisotropic Magnon Dispersion in Ca_2RuO_4: Evidence for Strong Spin-Orbit Coupling, Phys. Rev. Lett. **115**, 247201 (2015).

[25] S. Kunkemöller, E. Komleva, S. V. Streltsov, S. Hoffmann, D. I. Khomskii, P. Steffens, Y. Sidis, K. Schmalzl, and M. Braden, Magnon dispersion in $Ca_2Ru_{1-x}Ti_xO_4$: Impact of spin-orbit coupling and oxygen moments, Phys. Rev. B **95**, 214408 (2017).

[26] G. Zhang and E. Pavarini, Mott transition, spin-orbit effects, and magnetism in Ca_2RuO_4, Phys. Rev. B **95**, 075145 (2017).

[27] G. Zhang and E. Pavarini, Higgs mode and stability of $x$my $-$ orbital ordering in Ca_2RuO_4, Phys. Rev. B **101**, 205128 (2020).

[28] T. Feldmaier, P. Strobel, M. Schmid, P. Hansmann, and M. Daghofer, Excitonic magnetism at the intersection of spin-orbit coupling and crystal-field splitting, Phys. Rev. Res. **2**, 033201 (2020).

[29] B. J. Kim and G. Khaliullin, Resonant inelastic x-ray scattering operators for t_{2g} orbital systems, Phys. Rev. B **96**, 085108 (2017).

[30] C. G. Fatuzzo, M. Dantz, S. Fatale, P. Olalde-Velasco, N. E. Shaik, B. Dalla Piazza, S. Toth, J. Pelliciari, R. Fittipaldi, A. Vecchione, N. Kikugawa, J. S. Brooks, H. M. Rønnow, M. Grioni, Ch. Rüegg, T. Schmitt, and J. Chang, Spin-orbit-induced orbital excitations in Sr_2RuO_4 and Ca_2RuO_4:

A resonant inelastic x-ray scattering study, Phys. Rev. B **91**, 155104 (2015).

[31] L. Das, F. Forte, R. Fittipaldi, C. G. Fatuzzo, V. Granata, O. Ivashko, M. Horio, F. Schindler, M. Dantz, Y. Tseng, D. E. McNally, H. M. Rønnow, W. Wan, N. B. Christensen, J. Pelliciari, P. Olalde-Velasco, N. Kikugawa, T. Neupert, A. Vecchione, T. Schmitt *et al.*, Spin-Orbital Excitations in Ca$_2$RuO$_4$ Revealed by Resonant Inelastic X-Ray Scattering, Phys. Rev. X **8**, 011048 (2018).

[32] H. Gretarsson, H. Suzuki, Hoon Kim, K. Ueda, M. Krautloher, B. J. Kim, H. Yavaş, G. Khaliullin, and B. Keimer, Observation of spin-orbit excitations and Hund's multiplets in Ca$_2$RuO$_4$, Phys. Rev. B **100**, 045123 (2019).

[33] I. Vergara, M. Magnaterra, P. Warzanowski, J. Attig, S. Kunkemöller, D. I. Khomskii, M. Braden, M. Hermanns, and M. Grüninger, Spin-orbit coupling and crystal-field splitting in Ti-doped Ca$_2$RuO$_4$ studied by ellipsometry, Phys. Rev. B **106**, 085103 (2022).

[34] H. Takahashi, H. Suzuki, J. Bertinshaw, S. Bette, C. Mühle, J. Nuss, R. Dinnebier, A. Yaresko, G. Khaliullin, H. Gretarsson, T. Takayama, H. Takagi, and B. Keimer, Nonmagnetic $J = 0$ State and Spin-Orbit Excitations in K$_2$RuCl$_6$, Phys. Rev. Lett. **127**, 227201 (2021).

[35] B. Yuan, J. P. Clancy, A. M. Cook, C. M. Thompson, J. Greedan, G. Cao, B. C. Jeon, T. W. Noh, M. H. Upton, D. Casa, T. Gog, A. Paramekanti, and Y.-J. Kim, Determination of Hund's coupling in $5d$ oxides using resonant inelastic x-ray scattering, Phys. Rev. B **95**, 235114 (2017).

[36] M. Kusch, V. M. Katukuri, N. A. Bogdanov, B. Büchner, T. Dey, D. V. Efremov, J. E. Hamann-Borrero, B. H. Kim, M. Krisch, A. Maljuk, M. Moretti Sala, G. Aslan-Cansever, M. Sturza, L. Hozoi, J. van den Brink, and J. Geck, Observation of heavy spin-orbit excitons propagating in a non-magnetic background: The case of (Ba, Sr)$_2$YIrO$_6$, Phys. Rev. B **97**, 064421 (2018).

[37] A. Nag, S. Bhowal, A. Chakraborty, M. M. Sala, A. Efimenko, F. Bert, P. K. Biswas, A. D. Hillier, M. Itoh, S. D. Kaushik, V. Siruguri, C. Meneghini, I. Dasgupta, and S. Ray, Origin of magnetic moments and presence of spin-orbit singlets in Ba$_2$YIrO$_6$, Phys. Rev. B **98**, 014431 (2018).

[38] A. A. Aczel, Q. Chen, J. P. Clancy, C. dela Cruz, D. Reig-i-Plessis, G. J. MacDougall, C. J. Pollock, M. H. Upton, T. J. Williams, N. LaManna, J. P. Carlo, J. Beare, G. M. Luke, and H. D. Zhou, Spin-orbit coupling controlled ground states in the double perovskite iridates A_2BIrO$_6$ (A = Ba, Sr; B = Lu, Sc), Phys. Rev. Mater. **6**, 094409 (2022).

[39] A. Paramekanti, D. J. Singh, B. Yuan, D. Casa, A. Said, Y.-J. Kim, and A. D. Christianson, Spin-orbit coupled systems in the atomic limit: rhenates, osmates, iridates, Phys. Rev. B **97**, 235119 (2018).

[40] G. Cao, T. F. Qi, L. Li, J. Terzic, S. J. Yuan, L. E. DeLong, G. Murthy, and R. K. Kaul, Novel Magnetism of Ir^{5+}($5d^4$) Ions in the Double Perovskite Sr$_2$YIrO$_6$, Phys. Rev. Lett. **112**, 056402 (2014).

[41] J. Terzic, H. Zheng, F. Ye, H. D. Zhao, P. Schlottmann, L. E. De Long, S. J. Yuan, and G. Cao, Evidence for a low-temperature magnetic ground state in double-perovskite iridates with Ir^{5+}($5d^4$) ions, Phys. Rev. B **96**, 064436 (2017).

[42] S. Fuchs, T. Dey, G. Aslan-Cansever, A. Maljuk, S. Wurmehl, B. Büchner, and V. Kataev, Unraveling the Nature of Magnetism of the $5d^4$ Double Perovskite Ba$_2$YIrO$_6$, Phys. Rev. Lett. **120**, 237204 (2018).

[43] N. R. Davies, C. V. Topping, H. Jacobsen, A. J. Princep, F. K. K. Kirschner, M. C. Rahn, M. Bristow, J. G. Vale, I. da Silva, P. J. Baker, Ch. J. Sahle, Y.-F. Guo, D.-Y. Yan, Y.-G. Shi, S. J. Blundell, D. F. McMorrow, and A. T. Boothroyd, Evidence for a $J_{eff} = 0$ ground state and defect-induced spin glass behavior in the pyrochlore osmate Y$_2$Os$_2$O$_7$, Phys. Rev. B **99**, 174442 (2019).

[44] N. Iwahara and S. Shikano, Vibronic excitations in resonant inelastic x-ray scattering spectra of K$_2$RuCl$_6$, Phys. Rev. Res. **5**, 023051 (2023).

[45] A. Georges, L. de'Medici, and J. Mravlje, Strong correlations from Hund's coupling, Annu. Rev. Condens. Matter Phys. **4**, 137 (2013).

[46] J. E. Fergusson and P. F. Heveldt, The influence of π-bonding and steric factors on hexahalogeno-metallates, Aust. J. Chem. **27**, 661 (1974).

[47] R. L. Armstrong, D. Mintz, B. M. Powell, and W. J. L. Buyers, Ferrorotative transition in the antifluorite crystal K$_2$OsCl$_6$, Phys. Rev. B **17**, 1260 (1978).

[48] M. Saura-Múzquiz, M. Avdeev, H. E. A. Brand, and B. J. Kennedy, Structural and magnetic properties of some vacancy-ordered osmium halide perovskites, Inorg. Chem. **61**, 15961 (2022).

[49] L. J.P. Ament, M. van Veenendaal, T. P. Devereaux, J. P. Hill, and J. van den Brink, Resonant inelastic x-ray scattering studies of elementary excitations, Rev. Mod. Phys. **83**, 705 (2011).

[50] A. Gössling, R. Schmitz, H. Roth, M. W. Haverkort, T. Lorenz, J. A. Mydosh, E. Müller-Hartmann, and M. Grüninger, Mott-Hubbard exciton in the optical conductivity of YTiO$_3$ and SmTiO$_3$, Phys. Rev. B **78**, 075122 (2008).

[51] J. Reul, A. A. Nugroho, T. T. M. Palstra, and M. Grüninger, Probing orbital fluctuations in RVO$_3$ (R = Y, Gd, or Ce) by ellipsometry, Phys. Rev. B **86**, 125128 (2012).

[52] B. Henderson and G. F. Imbusch, *Optical Spectroscopy of Inorganic Solids* (Oxford, New York, 1989).

[53] B. N. Figgis and M. A. Hitchman, *Ligand Field Theory and its Applications* (Wiley, New York, 1999).

[54] R. Rückamp, E. Benckiser, M. W. Haverkort, H. Roth, T. Lorenz, A. Freimuth, L. Jongen, A. Möller, G. Meyer, P. Reutler, B. Büchner, A. Revcolevschi, S.-W. Cheong, C. Sekar, G. Krabbes, and M. Grüninger, Optical study of orbital excitations in transition-metal oxides, New J. Phys. **7**, 144 (2005).

[55] E. Benckiser, R. Rückamp, T. Möller, T. Taetz, A. Möller, A. A. Nugroho, T. T. M. Palstra, G. S. Uhrig, and M. Grüninger, Collective orbital excitations in orbitally ordered YVO$_3$ and HoVO$_3$, New J. Phys. **10**, 053027 (2008).

[56] E. Benckiser, L. Fels, G. Ghiringhelli, M. Moretti Sala, T. Schmitt, J. Schlappa, V. N. Strocov, N. Mufti, G. R. Blake, A. A. Nugroho, T. T. M. Palstra, M. W. Haverkort, K. Wohlfeld, and M. Grüninger, Orbital superexchange and crystal field simultaneously at play in YVO$_3$: Resonant inelastic x-ray scattering at the V L edge and the O K edge, Phys. Rev. B **88**, 205115 (2013).

[57] B. W. Lebert, S. Kim, V. Bisogni, I. Jarrige, A. M. Barbour, and Y.-J. Kim, Resonant inelastic x-ray scattering study of $\alpha -$ RuCl$_3$: a progress report, J. Phys.: Condens. Matter **32**, 144001 (2020).

[58] P. Warzanowski, N. Borgwardt, K. Hopfer, J. Attig, T. C. Koethe, P. Becker, V. Tsurkan, A. Loidl, M. Hermanns, P. H. M. van Loosdrecht, and M. Grüninger, Multiple spin-orbit excitons and the electronic structure of $\alpha - RuCl_3$, Phys. Rev. Res. **2**, 042007(R) (2020).

[59] H. Suzuki, H. Liu, J. Bertinshaw, K. Ueda, H. Kim, S. Laha, D. Weber, Z. Yang, L. Wang, H. Takahashi, K. Fürsich, M. Minola, B. V. Lotsch, B. J. Kim, H. Yavaş, M. Daghofer, J. Chaloupka, G. Khaliullin, H. Gretarsson, and B. Keimer, Proximate ferromagnetic state in the Kitaev model material $\alpha - RuCl_3$, Nat. Commun. **12**, 4512 (2021).

[60] B. A. Kozikowski and T. A. Keiderling, Intraconfigurational absorption spectroscopy of Os^{4+} ion in K_2SnCl_6 and K_2OsCl_6 crystals, J. Phys. Chem. **87**, 4630 (1983).

[61] A. Bertin, L. Kiefer, and M. Braden (private communication).

[62] G. A. Bain and J. F. Berry, Diamagnetic corrections and pascal's constants, J. Chem. Educ. **85**, 532 (2008).

[63] Y. Zhang, L.-F. Lin, A. Moreo, and E. Dagotto, $J = 0$ nonmagnetic insulating state in K_2OsX_6 ($X = F$, Cl, and Br), Phys. Rev. B **106**, 155148 (2022).

[64] M. W. Haverkort, M. Zwierzcki, and O. K. Andersen, Multiplet ligand-field theory using Wannier orbitals, Phys. Rev. B **85**, 165113 (2012).

[65] M. W. Haverkort, Quanty for core level spectroscopy - excitons, resonances and band excitations in time and frequency domain, J. Phys.: Conf. Ser. **712**, 012001 (2016).

[66] S. Huotari, G. Vankó, F. Albergamo, C. Ponchut, H. Graafsma, C. Henriquet, R. Verbeni, and G. Monaco, Improving the performance of high-resolution x-ray spectrometers with position-sensitive pixel detectors, J. Synchrotron Rad. **12**, 467 (2005).

[67] S. Huotari, F. Albergamo, G. Vankó, R. Verbeni, and G. Monaco, Resonant inelastic hard x-ray scattering with diced analyzer crystals and position-sensitive detectors, Rev. Sci. Instrum. **77**, 053102 (2006).

[68] M. Moretti Sala, C. Henriquet, L. Simonelli, R. Verbeni, and G. Monaco, High energy-resolution set-up for Ir L_3 edge RIXS experiments, J. Electron Spectrosc. Relat. Phenom. **188**, 150 (2013).

[69] M. Moretti Sala, K. Martel, C. Henriquet, A. Al Zein, L. Simonelli, Ch. J. Sahle, H. Gonzalez, M.-C. Lagier, C. Ponchut, S. Huotari, R. Verbeni, M. Krisch, and G. Monaco, A high-energy-resolution resonant inelastic X-ray scattering spectrometer at ID20 of the European Synchrotron Radiation Facility, J. Synchrotron Rad. **25**, 580 (2018).

[70] P. J. E. M. van der Linden, M. Moretti Sala, C. Henriquet, M. Rossi, K. Ohgushi, F. Fauth, L. Simonelli, C. Marini, E. Fraga, C. Murray, J. Potter, and M. Krisch, A compact and versatile dynamic flow cryostat for photon science, Rev. Sci. Instr. **87**, 115103 (2016).

[71] M. Minola, G. Dellea, H. Gretarsson, Y. Y. Peng, Y. Lu, J. Porras, T. Loew, F. Yakhou, N. B. Brookes, Y. B. Huang, J. Pelliciari, T. Schmitt, G. Ghiringhelli, B. Keimer, L. Braicovich, and M. Le Tacon, Collective Nature of Spin Excitations in Superconducting Cuprates Probed by Resonant Inelastic X-Ray Scattering, Phys. Rev. Lett. **114**, 217003 (2015).

[72] J. Reul, L. Fels, N. Qureshi, K. Shportko, M. Braden, and M. Grüninger, Temperature-dependent optical conductivity of layered $LaSrFeO_4$, Phys. Rev. B **87**, 205142 (2013).

[73] N. Borgwardt, J. Lux, I. Vergara, Z. Wang, A. A. Taskin, K. Segawa, P. H. M. van Loosdrecht, Y. Ando, A. Rosch,

and M. Grüninger, Self-organized charge puddles in a three-dimensional topological material, Phys. Rev. B **93**, 245149 (2016).

[74] R. M. A. Azzam and N. M. Bashara, *Ellipsometry and Polarized Light* (Elsevier, New York, 1987).

[75] M. Grüninger, M. Windt, T. Nunner, C. Knetter, K. P. Schmidt, G. S. Uhrig, T. Kopp, A. Freimuth, U. Ammerahl, B. Büchner, and A. Revcolevschi, Magnetic excitations in two-leg spin 1/2 ladders: Experiment and theory, J. Phys. Chem. Solids **63**, 2167 (2002).

[76] D. Reig-i-Plessis, T. A. Johnson, K. Lu, Q. Chen, J. P. C. Ruff, M. H. Upton, T. J. Williams, S. Calder, H. D. Zhou, J. P. Clancy, A. A. Aczel, and G. J. MacDougall, Structural, electronic, and magnetic properties of nearly ideal $J_{eff} = 1/2$ iridium halides, Phys. Rev. Mater. **4**, 124407 (2020).

[77] A. Paramekanti, D. D. Maharaj, and B. D. Gaulin, Octupolar order in d-orbital Mott insulators, Phys. Rev. B **101**, 054439 (2020).

[78] S. W. Lovesey and D. D. Khalyavin, Lone octupole and bulk magnetism in osmate $5d^2$ double perovskites, Phys. Rev. B **102**, 064407 (2020).

[79] G. Khaliullin, D. Churchill, P. P. Stavropoulos, and H.-Y. Kee, Exchange interactions, Jahn-Teller coupling, and multipole orders in pseudospin one-half $5d^2$ Mott insulators, Phys. Rev. Res. **3**, 033163 (2021).

[80] S. Voleti, A. Haldar, and A. Paramekanti, Octupolar order and Ising quantum criticality tuned by strain and dimensionality: Application to d-orbital Mott insulators, Phys. Rev. B **104**, 174431 (2021).

[81] L. V. Pourovskii, D. F. Mosca, and C. Franchini, Ferro-octupolar order and low-energy excitations in d^2 double perovskites of osmium, Phys. Rev. Lett. **127**, 237201 (2021).

[82] A. Rayyan, D. Churchill, and H.-Y. Kee, Field-induced Kitaev multipolar liquid in spin-orbit coupled d^2 honeycomb Mott insulators, Phys. Rev. B **107**, L020408 (2023).

[83] H. Homborg, Absorptions- und elektronische Raman-Spektren von Intrakonfigurationsübergängen der Hexahalogenokomplexe von Os^{IV} ($X = Cl$, I) und Ir^{IV} ($X = Cl$, Br), Z. Anorg. Allg. Chem. **493**, 121 (1982).

[84] D. Mintz, R. L. Armstrong, B. M. Powell, and W. J. L. Buyers, Soft rotary mode in the antifluorite crystal K_2OsCl_6, Phys. Rev. B **19**, 448 (1979).

[85] G. P. O'Leary and R. G. Wheeler, Phase transitions and soft librational modes in cubic crystals, Phys. Rev. B **1**, 4409 (1970).

[86] N. Khan, D. Prishchenko, M. H. Upton, V. G. Mazurenko, and A. A. Tsirlin, Towards cubic symmetry for Ir^{4+}: Structure and magnetism of the antifluorite K_2IrBr_6, Phys. Rev. B **103**, 125158 (2021).

[87] A. Bertin, T. Dey, D. Brüning, D. Gorkov, K. Jenni, A. Krause, P. Becker, L. Bohatý, D. Khomskii, M. Braden, and T. Lorenz, Interplay of weak ferromagnetism, ferroelasticity and shape-memory effects in the spin-orbit coupled antiferromagnet K_2ReCl_6, arXiv:2207.11101

[88] B. A. Kozikowski and T. A. Keiderling, Intraconfigurational absorption and magnetic circular dichroism spectra of Os^{4+} in Cs_2ZrCl_6 and in Cs_2ZrBr_6, Mol. Phys. **40**, 477 (1980).

[89] H. U. Rahman, Analysis of the Magnetic Susceptibility of K_2OsCl_6, Phys. Rev. B **3**, 729 (1971).

[90] P. B. Dorain, H. H. Patterson, and P. C. Jordan, Optical spectra of Os^{4+} in single cubic crystals at 4.2 °K, J. Chem. Phys. **49**, 3845 (1968).

[91] S. B. Piepho, J. R. Dickinson, J. A. Spencern, and P. N. Schatz, High resolution absorption and magnetic circular dichroism spectra of Cs_2ZrCl_6: Os^{4+}, Mol. Phys. **24**, 609 (1972).

[92] Y. Moritomo and Y. Tokura, Charge-transfer type excitations in layered cupric halides, Jpn. J. Appl. Phys. **32**, 344 (1993).

[93] R.-P. Wang, B. Liu, R. J. Green, M. U. Delgado-Jaime, M. Ghiasi, T. Schmitt, M. M. van Schooneveld, and F. M. F. de Groot, Charge-transfer analysis of $2p3d$ resonant inelastic X-ray scattering of cobalt sulfide and halides, J. Phys. Chem. C **121**, 24919 (2017).